Autonomous dynamic control of DNA nanostructure self-assembly

Leopold N. Green[1,2,9], Hari K. K. Subramanian [ID][3,9], Vahid Mardanlou[4], Jongmin Kim[5,6],
Rizal F. Hariadi[7] and Elisa Franco [ID][3,8]*

Biological cells routinely reconfigure their shape using dynamic signalling and regulatory networks that direct self-assembly processes in time and space, through molecular components that sense, process and transmit information from the environment. A similar strategy could be used to enable life-like behaviours in synthetic materials. Nucleic acid nanotechnology offers a promising route towards this goal through a variety of sensors, logic and dynamic components and self-assembling structures. Here, by harnessing both dynamic and structural DNA nanotechnology, we demonstrate dynamic control of the self-assembly of DNA nanotubes—a well-known class of programmable DNA nanostructures. Nanotube assembly and disassembly is controlled with minimal synthetic gene systems, including an autonomous molecular oscillator. We use a coarse-grained computational model to capture nanotube length distribution dynamics in response to inputs from nucleic acid circuits. We hope that these results may find use for the development of responsive nucleic acid materials, with potential applications in biomaterials science, nanofabrication and drug delivery.

Biological systems use non-equilibrium self-assembly for growth, self-repair and transport[1]. For example, the cytoskeleton controls cell shape[2], chromosomal separation[3,4] and mobility[5] owing to dynamic signalling and regulatory networks directing self-assembly in time and space. By embedding similar architectures in synthetic materials, we should be able to build adaptive matter with the capacity for logic and autonomous behaviours. However, natural biomolecular assembly systems are very complex and are difficult to reconstitute and reprogram—an alternative route is offered by reductionist, cell-free approaches relying on modular molecular parts that can be rationally engineered[6].

Nucleic acid nanotechnology has developed a multitude of programmable self-assembling systems[7] as well as sensors and logic and dynamic networks[8,9] that have the potential to operate together to build responsive materials. The well understood thermodynamic properties of Watson–Crick base pair interactions make it possible to design self-assembling structures and circuits by specifying domain-level assembly patterns, and by subsequently identifying optimal sequences with computational tools[10,11]. A growing number of design methods in structural DNA nanotechnology, such as DNA tiles[12–14], DNA origami[15,16], DNA bricks[17], wireframe structures[18,19] and crystals[20], allow the construction of molecular objects with controlled nanoscale features, and size ranging from a few nanometres to hundreds of micrometres. These programmable structures can be used as scaffolds for a variety of ligands[21]. In parallel, building on the principle of toehold-mediated branch migration[22], dynamic DNA nanotechnology has produced multilayered circuits that can include more than 100 DNA strands[23–25]. Nucleic acid circuits can sense a number of environmental triggers[26] and can be powered by enzymatic reactions enabling autonomous (non-equilibrium) dynamics such as bistability and oscillations[27–30].

Here, we demonstrate the tunable and reversible dynamic control of self-assembly of DNA tubular structures, bridging structural and dynamic DNA nanotechnology. These DNA nanotubes assemble from nanoscale tiles, reaching up to tens of micrometres in length[12–14,31]. Using the principles of strand displacement, we build reactions that achieve isothermal control of nanotube assembly and disassembly using nucleic acid molecules. We show that these molecules can be produced by rationally designed transcriptional systems, and in particular by an autonomous transcriptional oscillator serving as an elementary clocking mechanism. Earlier steps towards the control of DNA tile self-assembly using DNA circuits focused exclusively on triggering nanostructure growth upon release of a DNA input molecule[32,33], a non-autonomous and non-reversible reaction. Recently, reversible nanostructure assembly in response to a pH sensor was demonstrated building on the results presented here[34]. We identify several general challenges to the bottom-up construction of autonomous biomolecular materials, in particular the difficulty of predicting assembly kinetics, the presence of undesired and often unknown interactions between interconnected components, and the limitation of resources in a closed system.

We hope that these results may find use for the development of responsive materials[35], and perhaps also in endeavours to generate artificial life with active spatial control[36]. Our demonstration builds on the availability of a myriad of components developed by nucleic acid nanotechnology, which could be interconnected to build active, programmable nucleic acid materials. Aptamer components could sense and transduce a variety of inputs (such as light intensity, temperature or the concentration of proteins, small molecules and nanoparticles[8,37]). Sensed signals could be logically or dynamically processed by nucleic acid circuits[9], whose outputs could, in turn, direct self-assembly of nucleic acid nanostructures[7]. Self-regulation
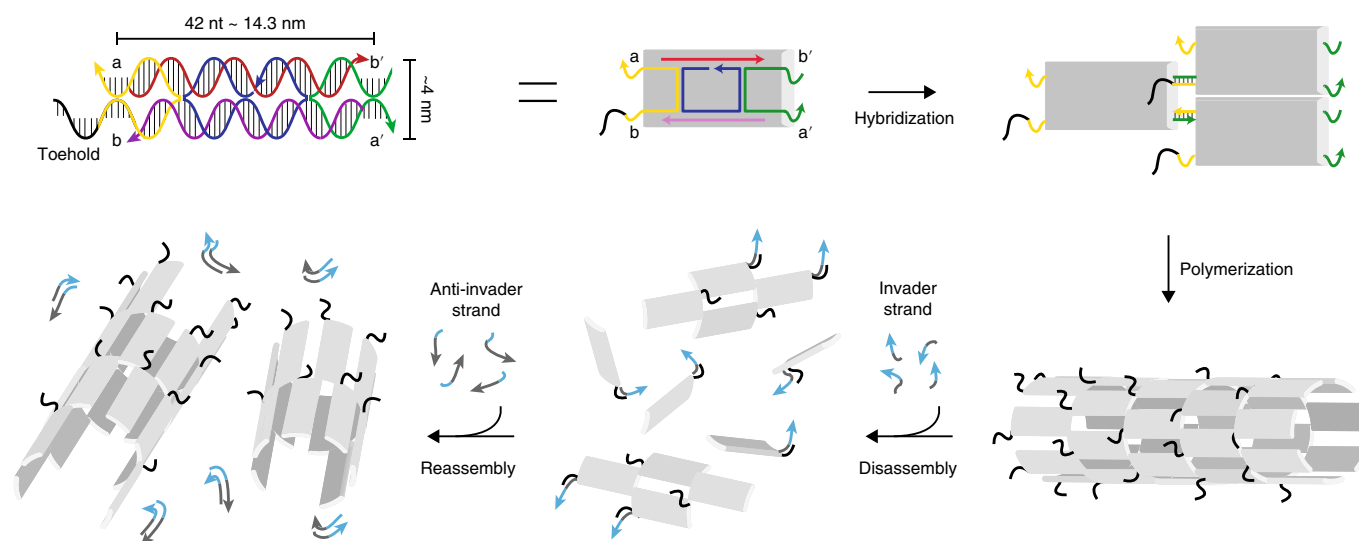
Fig. 1 | Schematics of DNA nanotube self-assembly and proposed control mechanisms. We consider DNA double-crossover tiles[12,14] formed by five unique DNA strands. Tiles assemble into nanotubes via programmed interactions of their sticky ends (domains marked a, b, a' and b'). In all sketches, the 3' ends are marked with an arrow. From top left, tiles were modified to include a single-stranded overhang, or toehold, illustrated as the black domain on the 5' end of the yellow strand. Tiles can be schematically represented as molecular bricks with complementary connectors. Hybridization of sticky ends results in the formation of hollow nanotubes with an average diameter of 13.5 nm (ref. [14]); toeholds placed on the 5' end of the yellow strand are expected to be on the external surface of the nanotube (conversely, toeholds on the 3' end of the yellow strand would be internal to the nanotube). The presence of a toehold makes the neighbouring sticky end accessible for strand invasion: an invader molecule complementary to the toehold and the sticky end domain invades one of the inter-tile bonds, causing the nanotubes to disassemble and making tiles inactive. If it includes an additional toehold domain, the invader strand can be displaced by an anti-invader strand, which reactivates tiles, enabling their reassembly into nanotubes.

and homeostasis of DNA nanostructure properties may be obtained by introducing feedback[38], where information on the structure growth or assembly state would control the signal-processing components. Because nucleic acid systems are, in general, designed modularly by specifying domain-level interactions, we envision that it will be possible to swap components and build scalable active materials with easily reconfigurable responses.

Results and discussion

Reversible nanotube assembly directed by programmable nucleic acid reactions. We demonstrate a responsive nucleic acid material, in which individual nanoscale monomers are controlled via strand invasion reactions that determine assembly or disassembly of the material components. We engineered double-crossover DNA tiles known as DAE-E[12,14], which include five distinct strands and assemble via sticky end interactions yielding hollow tubular structures. These nanotubes have a mean diameter of 13.5 nm (or 6–8 tile circumferences), and their persistence length has been estimated to be 4 μm (ref. [14]); in comparison, microtubules have a diameter of 24–33 nm (or 8–19 monomer circumferences) and a persistence length of 5.2×10^3 μm (refs. [39–41]). Formation of nanotubes is achieved by designing the tiles in such a way that the number of base pairs between inter-tile crossover points produces an angle between two adjacent tiles[14]. After tile nucleation[42,43], nanotubes polymerize[44,45] and join end-to-end[31], yielding populations of nanotubes with a maximum observed length that is on the order of tens of micrometres.

DAE-E tiles were modified at one of their sticky ends to include a seven-nucleotide toehold domain (black domain on the 5' end of the yellow strand in Fig. 1), which was chosen to protrude on the external surface of the nanotubes (Supplementary Section 2.4). The toehold serves as a binding domain to initiate strand invasion of the sticky ends: a single-stranded 'invader' molecule (blue-grey strand with blue arrow in Fig. 1) is designed to be complementary to the toehold and the sticky end sequences (12 nucleotides), to which it

binds, causing dissociation of one of the inter-tile bonds. Invasion of a single sticky end domain weakens tile–tile interactions enough to cause the nanostructure to collapse. Tiles bound to the invader become 'inactive'. Invader molecules are in turn designed to include a toehold domain, so that a complementary anti-invader strand can displace the invader and restore the ability of the tiles to self-assemble (Fig. 1). This allows control of the fraction of active tiles (isothermally and reversibly), thereby directing assembly and disassembly of the nanotubes.

Addition of invader strands causes disassembly of nanotubes within minutes, while addition of anti-invaders causes nanotubes to regrow to pre-invasion length with a timescale on the order of 1–2 h. To rapidly quantify nanotube length via fluorescence microscopy, tiles were labelled with fluorescent dyes, then annealed at 1 μM concentration using standard protocols (Supplementary Section 3.1) and incubated at room temperature. Example fluorescence microscopy images of nanotubes before invasion, after invasion and after anti-invasion are shown in Fig. 2a(i), top. Atomic force microscopy (AFM) images of the same samples (Fig. 2a(i), bottom) confirm the nanoscale features of the tubular assemblies and indicate that invasion causes nanotubes to collapse into small lattice fragments whose size does not exceed 500 nm. Fluorescence microscopy images were automatically processed (Supplementary Section 3.4) to gather the statistics of nanotube length at different times during the invasion and anti-invasion reactions. Normalized example histograms are shown in Fig. 2a(ii) (no histogram is reported for invaded nanotubes, because no nanotube is visible in the fluorescence microscopy images). After anti-invasion, nanotube growth is associated with a decrease in the number of nanotubes counted, consistent with the presence of joining reactions[31]. Length data from triplicate experiments were used to plot the mean nanotube length versus time in various reaction conditions, which were monitored for 30 h. Complete data sets and violin plots of individual experiments are provided in Supplementary Section 4.7 (Supplementary Figs. 25–28).
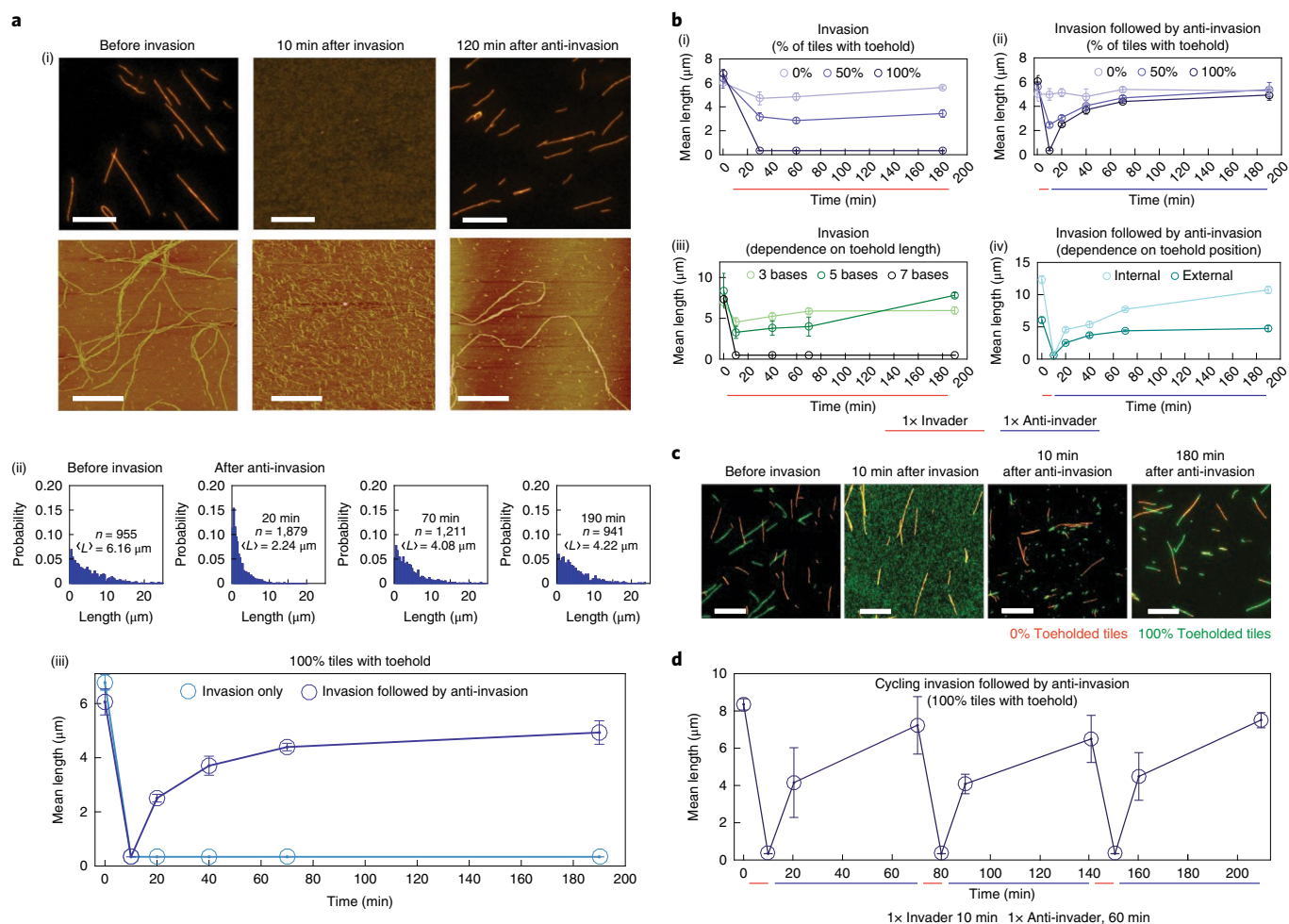
Fig. 2 | Control of DNA nanotube length distribution via strand invasion and displacement reactions. a, (i) Fluorescence microscopy images (top) and AFM images (bottom) of nanotubes before invasion (left), post invasion (middle) and post anti-invasion (right) reactions. Nanotubes labelled with Cy3 dye were imaged at 50 nM concentration. Scale bars, 10 μm (fluorescence microscopy images, top) and 2 μm (AFM images, bottom). (ii) Histograms of nanotube length measured from fluorescence microscopy images, before invasion and after anti-invasion (no nanotubes are visible after invasion); <L> indicates mean nanotube length. (iii) Mean length of nanotubes annealed with 100% toeholded tiles; the mean is computed over triplicate experiments, and error bars are the s.d. of mean length measured in each experiment. Nanotubes are disassembled and remain in a disassembled state after addition of invader (light blue). After addition of anti-invader, nanotubes reach ~5 μm mean length (dark blue). **b**, (i) Invasion of nanotubes annealed with no toeholded tiles has no significant effect on mean length; invasion of nanotubes with 50% toeholded tiles causes their mean length to halve, and nanotubes with 100% toeholded tiles break completely. (ii) Anti-invasion of disassembled nanotubes having 50% and 100% toeholded tiles promotes regrowth that achieves the pre-invasion mean value in ~3 hours. Nanotubes with 0% toeholded tiles are largely unaffected by the addition of invader and anti-invader. (iii) The tile toehold length determines the effectiveness of disassembly. A seven-base-long toehold allows the invader to disassemble nanotubes, preventing regrowth; three- and five-base-long toeholds enable disassembly, but spontaneous regrowth occurs. (iv) Invasion and anti-invasion reactions of nanotubes with toeholds protruding on the external or internal surface (3′ end of the yellow strand, cf. Fig. 1). Internal toeholds appear to promote faster growth and the formation of longer nanotubes, relative to nanotubes with external toeholds. **c**, Nanotube populations with toeholded (green, Alexa 488-labelled) and non-toeholded tiles (orange, Cy3-labelled) can be selectively invaded and anti-invaded (tiles are otherwise identical in this experiment). Invasion disassembles only green nanotubes, and anti-invasion restores their formation (and joining of green and orange nanotubes). Scale bars, 10 μm. **d**, Invasion and anti-invasion reactions can be sequentially repeated multiple times, controlling the nanotube length over time (bound invader and anti-invader form an inert complex whose concentration increases during this experiment). In **a**(iii), **b** and **d**, mean and s.d. of the mean of nanotube length are calculated over triplicate experiments.

Before initiating the invasion reaction, nanotubes were annealed and allowed to grow at room temperature for 30 h (reaching a mean length of ~6 μm). When invader is added in a stoichiometric amount relative to the total tile concentration, nanotubes disassemble within minutes and growth is inhibited (Fig. 2a(iii)). When anti-invader is added, nanotubes regrow to a mean length of 4.08 μm after 70 min; this growth rate appears slightly faster than what is observed in isolated nanotubes[31], presumably because the small lattices observed in invaded nanotube samples reduce

the energetic barriers to nucleation[42]. Agarose gel electrophoresis (Supplementary Fig. 30) and bulk fluorimetry (Supplementary Fig. 40) control experiments confirm the observations made with fluorescence microscopy and AFM.

Invasion and anti-invasion reactions can be programmed by systematic tuning of toeholded tile fraction, toehold length and toehold location. When tiles do not include a toehold domain, invasion of bound sticky end domains is unlikely to occur; however, invader can weakly bind to free tiles in solution, thereby slowing

down polymerization and causing a slight decrease in mean length (Fig. 2b(i)). If 50% of the tile population includes a toehold, the mean nanotube length decreases by about 50% and growth is suppressed unless anti-invader is supplied, as shown in Fig. 2b(ii). Toehold length influences the effectiveness of invasion in a similar manner: Fig. 2b(iii) shows that three- and five-nucleotide-long toeholds enable 30% and 60% mean length reduction, respectively. However, regrowth is not suppressed as effectively as in the presence of a longer toehold, presumably because of a higher dissociation rate of the invader–tile complex. Finally, by appending the toehold to the 3′ end of the yellow strand (instead of the 5′ end), it is possible to make it protrude on the internal surface of the nanotube (instead of on its external surface): therefore, toeholds are expected to be primarily accessible near the nanotube ends. As shown in Fig. 2b(iv), nanotubes with internal toehold reach twice the mean length of nanotubes with external toeholds (for reasons yet to be elucidated). The effects of invasion and anti-invasion reactions on the mean length of these nanotubes are qualitatively comparable to those observed for nanotubes with external toeholds. Time-lapse microscopy movies indicate that, as expected, invasion causes nanotubes with internal toeholds to mostly depolymerize from their ends, rather than breaking in the middle (Supplementary Movies 1–7).

When mixing populations of nanotubes that only differ in the presence or absence of toeholded tiles, invasion and anti-invasion reactions selectively target the toeholded nanotube population. Figure 2c presents example images of toeholded nanotubes in green (labelled with Alexa 488) mixed with non-toeholded nanotubes in orange (labelled with Cy3) before and after adding invader strand, which exclusively causes green nanotubes to disassemble. Addition of anti-invader restores the assembly of green nanotubes. It should be easy to demonstrate that distinct invaders may selectively target specific populations of nanotubes simultaneously present in the sample, as long as they present distinct toeholds, because sequence mismatches largely prevent toehold-mediated branch migration from proceeding[46].

Invasion and anti-invasion reactions can be subsequently repeated in the same nanotube sample, yielding comparable decrease and increase of mean nanotube length at each cycle. Figure 2d shows the results of triplicate experiments where aliquots of invader and anti-invader were added during three separate cycles of reaction. In each cycle, invader and anti-invader bind and form a fully double-stranded 'waste' species that does not further react with other components. Overall, these results show that toehold-mediated strand displacement, a programmable biochemical reaction, can be used to direct self-assembly of large nanostructures isothermally and reversibly, by controlling active binding sites of the monomer units.

Co-transcriptional control of nanotube assembly. In biological cells, gene networks are responsible not only for the production of assembling components, but also for the regulation of self-assembly pathways. For example, cells produce actin and tubulin as well as a variety of proteins that control the binding and activity of actin and tubulin, thereby determining cytoskeletal dynamics[4,47]. To embed the same architecture in our synthetic DNA material, we used a stripped-down, artificial version of gene expression pathways to control self-assembly of our DNA nanotubes. In vitro transcriptional networks are composed of linear DNA templates or 'genelets', DNA activators and inhibitors, and RNA transcripts that serve as triggerable regulators[27,28]. This toolkit relies on two enzymes, bacteriophage T7 RNA polymerase (RNAP) for RNA production and RNase H for RNA degradation. The promoter in each genelet is partially single-stranded; T7 RNAP can bind and transcription can occur only when the promoter is completed by hybridization of an 'activator' DNA strand (Fig. 3a). The activator can be designed to include a toehold, so that it can be displaced by a complementary

'inhibitor' DNA or RNA strand, thereby switching off transcription as shown in Fig. 3a, bottom[48].

Because genelet systems operate at 37 °C and require the presence of transcription mix (transcription buffer, high concentration of nucleoside triphosphates (NTPs) and high concentration of T7 RNA polymerase; see Methods and Supplementary Section 3.2), we developed a tile variant that can assemble into nanotubes under these experimental conditions. We extended the sticky ends of the tiles (without modifying the inter-tile crossover distance) to be eight nucleotides long to increase the nanotube melting temperature. These assemblies are also resilient to RNA products transcribed by T7 RNAP from the nanotubes, which cause nanotubes to disassemble, as recently shown by our group and others[49] (evidence of nanotube disassembly is provided in Supplementary Figs. 38 and 39). T7 RNAP-mediated disruption of DNA nanostructures due to non-specific transcription has been observed previously[50].

We designed a genelet whose RNA transcript works as an RNA invader: as shown in the reaction diagram in Fig. 3b, in the presence of activator the genelet is turned on and invader is produced at a rate that depends on the concentration of RNA polymerase and active genelet. Invader binds to the nanotubes and causes them to disassemble. In the presence of RNase H, RNA invader bound to DNA tiles is degraded, thereby making it possible for tiles to reassemble. If the genelet is switched off (no invader is produced), RNase H degradation becomes predominant and promotes nanotube regrowth.

Figure 3c shows the mean length of nanotubes that are co-transcriptionally invaded in the presence of RNase H (dark blue): nanotubes disassemble rapidly and do not regrow. The mean length of nanotubes incubated in the same transcriptional conditions, but in the absence of invader genelet, remains roughly constant. If the genelet is deactivated by adding inhibitor strand, invader transcription is switched off and RNase H degradation promotes nanotube regrowth, as shown in Fig. 3d.

Autonomous control of nanotube assembly using a synthetic oscillator. Biological scaffolds such as the cytoskeleton need to reconfigure periodically during cell division, suggesting that there is direct or indirect coupling between the self-assembling components and circadian rhythms[51,52]. Furthermore, a clocking mechanism is required for the continuous autonomous behaviour of many engineered systems. This inspired us to endeavour to direct the assembly and disassembly of the nanotube system using a synthetic molecular oscillator.

Because it was possible to control nanotube assembly using transcription, we selected a programmable genelet oscillator[28,50,53] and identified an appropriate architecture to couple this complex chemical reaction with the self-assembling nanotubes. This transcriptional oscillator is composed of two mutually regulating transcriptional switches SW12 and SW21. These switches are composed of a genelet, its activators and inhibitors (input), and its RNA transcript (output). As shown in Fig. 4, the output of switch SW12 is an RNA activator (rA1) that turns on switch SW21; in turn, SW21 produces an RNA inhibitor (rI2) that turns off SW12. Activation and inhibition occur via toehold-mediated branch migration; a complete reaction scheme is provided in Supplementary Section 2.6 (Supplementary Figs. 7–10). T7 RNAP and RNase H respectively produce and degrade RNA, as previously mentioned. Oscillations arise because the interconnected topology of the switches constitutes a negative feedback loop, where titration of inhibitors and activators introduces the appropriate nonlinearities[54]. Oscillations are measured in bulk fluorimetry experiments, where we track the state of SW21 via a fluorophore/quencher pair (Supplementary Section 4.13).

To couple the oscillator and the nanotubes we used an 'insulator' genelet, which serves as a buffering element. A direct interconnection of the oscillator and a downstream molecular 'load' would
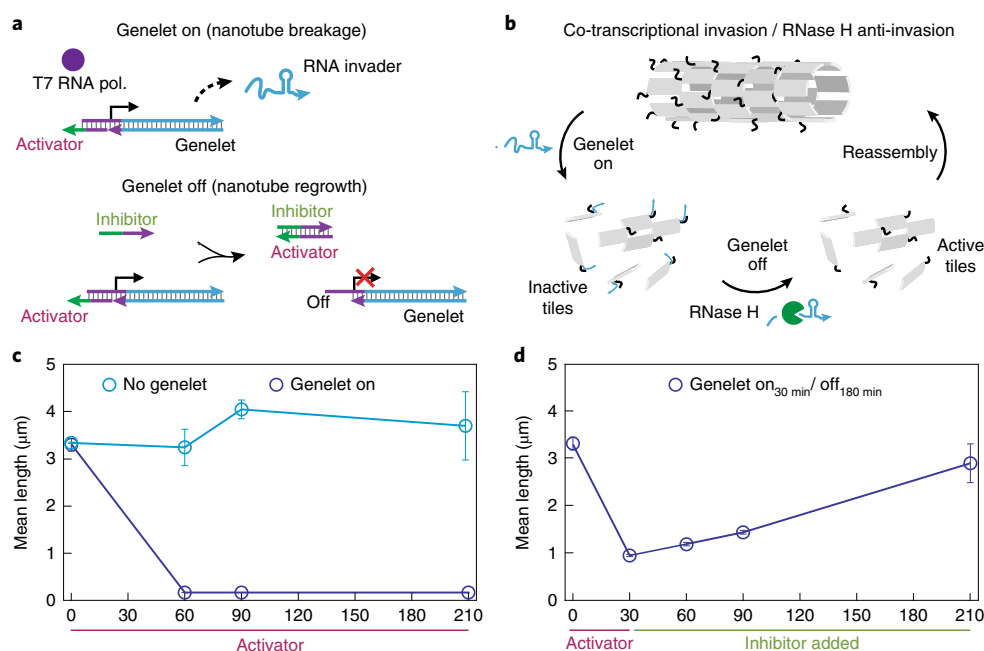
Fig. 3 | Transcriptional control of nanotube self-assembly. a, A synthetic transcriptional template, or genelet, is on when the incomplete T7 promoter domain is bound to the activator strand. In the presence of T7 RNA polymerase, RNA invader is produced (top). The genelet is turned off by toehold-mediated displacement of activator by a DNA inhibitor strand (bottom). **b**, Reaction scheme of co-transcriptional invasion of nanotubes; when the genelet producing invader is turned off, RNase H degradation of RNA invader bound to tiles becomes predominant and promotes nanotube regrowth. **c**, Co-transcriptional invasion of toeholded DNA nanotubes engineered to be resilient to the transcriptional environment (eight-base-long sticky ends). In the absence of genelet, but in the presence of RNAP and RNase H and transcription conditions, the mean nanotube length remains constant (light blue). In the presence of genelet on, nanotubes break and remain disassembled (dark blue). **d**, If the genelet is switched off (after 30 min from the beginning of the experiment), RNase H degradation dominates the reaction and promotes nanotube regrowth. In **c** and **d**, the mean and s.d. of the mean of nanotube length are calculated over triplicate experiments.
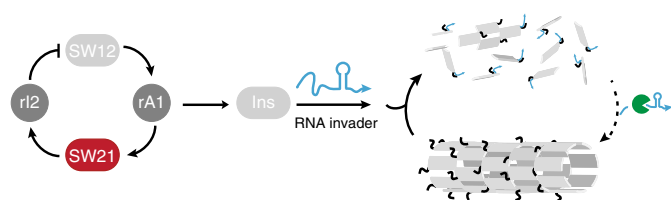

Fig. 4 | Schematic of a system in which nanotube assembly is directed by a synthetic molecular oscillator. We used a synthetic transcriptional oscillator to direct invasion of DNA nanotubes. The output of switch SW12 is the RNA activator rA1, which turns on switch SW21; in turn, SW21 produces an RNA inhibitor (rI2) that turns off switch SW12 (bar-headed arrow). The oscillator is coupled to an insulator genelet (Ins), which produces RNA invader. The insulator genelet is on when SW21 is on; thus, the invader production rate reaches its maximum when SW21 is fully active, and nanotubes are expected to break. When SW21 is inactive, the invader production rate is low and RNase H degradation promotes nanotube regrowth.

result in consumption of oscillator components and consequent perturbation of the reaction dynamics up to complete loss of oscillations[50]. This effect is also known as retroactivity[55], and can be mitigated by an amplification device. The insulator genelet serves precisely this purpose: it is directed by a small amount of the same molecules regulating switch SW21, and produces a large amount of RNA transcript designed to be an invader for the nanotubes. During an oscillation cycle, the fraction of active SW21 and the fraction of active insulator are expected to exhibit the same dynamics. When

the SW21 and insulator components are active (peaks of the oscillations) the invader concentration increases and nanotubes break. When SW21 and insulator activity are low (wells of the oscillations), the concentration of invader decreases and RNase H degradation of invader in the invader–tile complexes dominates, thereby promoting nanotube reassembly. In other words, the nanotube growth is anti-correlated to SW21 activity. Because the anti-invasion reaction depletes RNase H, which is present in solution in a finite amount, this reaction can significantly perturb the oscillator dynamics. The additional transcriptional load on RNAP due to the presence of insulator is minor, given the typical operating conditions of the system[50]. Yet, non-specific transcription by RNAP from DNA nanotubes has an impact on how much RNAP is available for the oscillator reactions[49]. For this reason, to obtain oscillatory kinetics in the desired range, the concentration of oscillator components and enzymes must be calibrated in the presence of DNA nanotubes.

Because nanotube growth proceeds at a limited rate, our first goal was to tune the oscillator to exhibit a period of 1–3 h and high amplitude. When the oscillator is in isolation, amplitude and period can be modulated (although not independently) by choosing concentrations of oligonucleotides and enzymes. The dynamics are particularly sensitive to the enzyme activity[53], and require fast transcription and degradation reactions. Because enzymes were purchased off the shelf, our ability to tune the oscillator kinetics was constrained by the availability of highly active RNAP and RNase H. In addition, this oscillator operates in a closed system and, consequently, the reactions cannot be sustained for more than 15–20 h due to reduction of enzyme activity, accumulation of incompletely degraded RNA and consumption of NTPs[28,50]. As a consequence, amplitude and frequency are time-varying. Given all these challenges, we were able to tune the oscillator to exhibit one or two
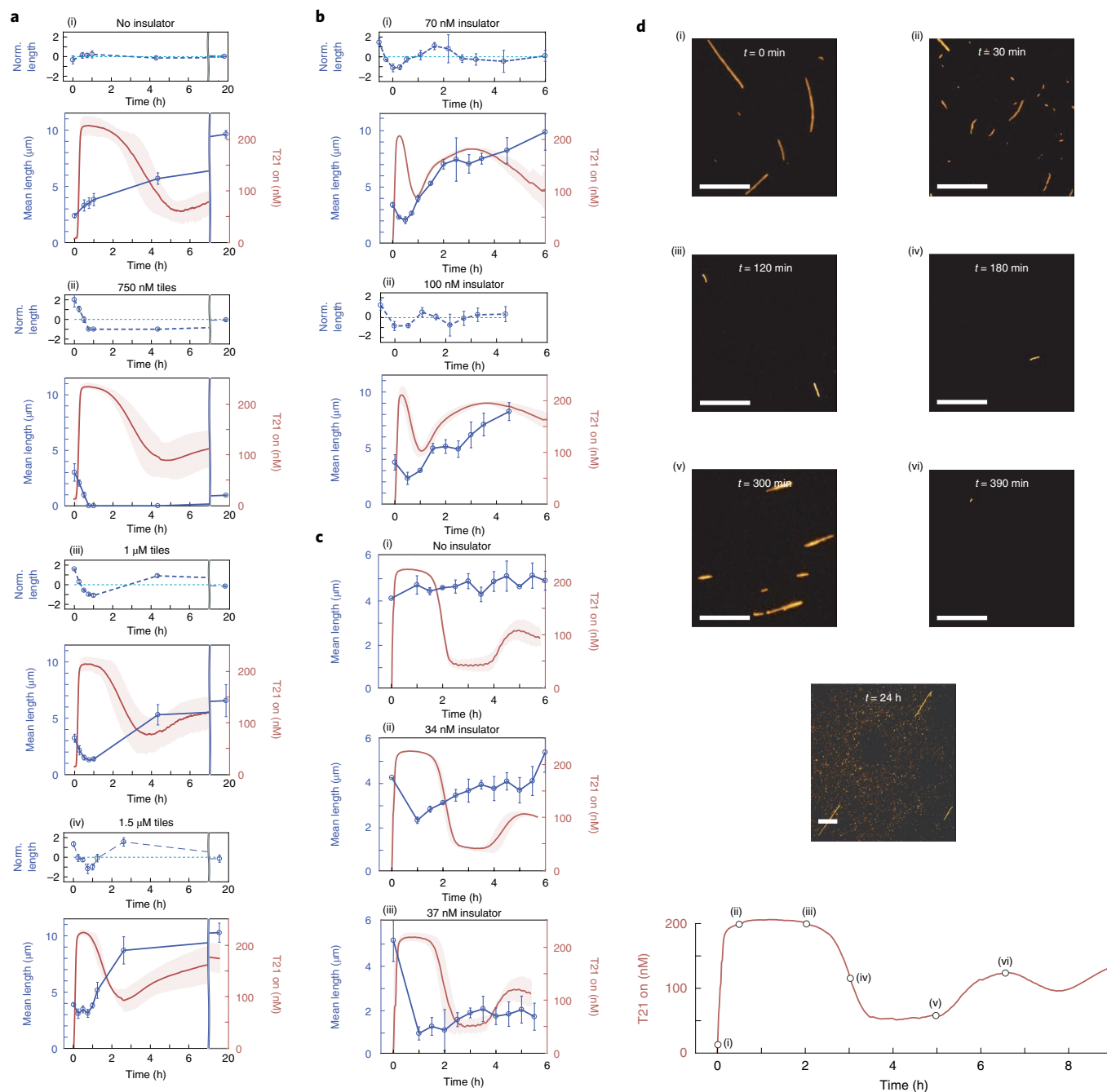
Fig. 5 | Controlling nanotube self-assembly with a molecular oscillator. Experiments demonstrating that nanotube assembly and disassembly can be directed over time using the molecular oscillator as described in Fig. 4. Fluorimetry experiments report the fraction of active SW21 (red node in Fig. 4). **a**, In a first round of experiments we tuned the oscillator to exhibit a single, high-amplitude, slow pulse. Active SW21 is shown in red and nanotube mean length in blue. The normalized nanotube mean length is shown above each figure; normalization was done by subtracting an exponential growth curve fitted to the mean length data (Supplementary Section 5.2.1). (i) In the absence of insulator (Ins), the nanotube mean length increases throughout the experiment (tile concentration 1 μM). In the presence of 65 nM insulator, we varied the total tile concentration. (ii) At 750 nM tile concentration, as SW21 becomes active, nanotubes disassemble and do not regrow. (iii) At 1 μM tile concentration, the nanotube mean length decreases as SW21 turns on, and increases as SW21 turns off. (iv) At 1.5 μM tile concentration we observe a trend similar to the 1 μM tile case, although the initial decrease in mean length is moderate. The oscillator behaviour is affected by a high concentration of tiles, because invader-bound tiles sequester RNase H. **b**, (i,ii) In a second round of experiments, we tuned the oscillator to exhibit two faster oscillations, and we varied the concentration of insulator at 1 μM tile concentration. At 70 nM (i) and 100 nM (ii) insulator concentration, the nanotube mean length decreases at the first peak of the SW21, increases in correspondence of the first well, and stalls for over 1 hour as SW21 reaches its second peak (for additional data see Supplementary Fig. 52). **c**, (i) A third round of experiments were carried out using a nanotube variant whose mean length does not increase significantly when incubated with the oscillator in the absence of insulator. (ii,iii) In the presence of insulator, the nanotube mean length decreases when SW21 turns on, it increases as SW21 is switched off, and it stalls as SW21 switches back on; these changes in mean length are more prominent as the insulator concentration increases. **d**, As part of experiment round 3, at 40 nM insulator the number of nanotubes is low after the first peak of SW21; representative images show that few short nanotubes are visible at the peaks of SW21 (ii,iii,vi), while several long nanotubes are visible at the end of the first well (v) and after overnight incubation. In all images the scale bar is 10 μm. Additional representative images and a repeat are reported in Supplementary Figs 57–59. In **a**, **b** and **c**, mean and s.d. of the mean of nanotube length and the SW21 active fraction are calculated over triplicate experiments.

large-amplitude oscillations while directing the nanotube system. The oscillator was tuned by primarily varying the concentrations of distinct enzyme batches, as described in detail in Supplementary Section 4.13.

In our first series of experiments (experiment round 1) we assessed the behaviour of the system when the total tile concentration is varied. We focused on the single-oscillation operating point, which exhibits a high-amplitude pulse that slowly dampens after 6 h; this operating point was easier to achieve repeatedly, and evolves on a timescale largely comparable to that observed in co-transcriptionally controlled nanotubes (Fig. 5a). First, we measured the nanotube mean length when nanotubes are grown in the oscillator sample in the absence of insulator that couples nanotube self-assembly to the oscillator dynamics. We observed that nanotubes incubated in the oscillator mix become unusually long, a phenomenon we have not yet explained. To account for the increased nanotube growth, in all oscillator experiments we normalized nanotube length data by subtracting a phenomenologically fitted exponential function that captures the growth rate, as explained in Supplementary Section 5.1. Normalized mean length data are shown on top of the mean length data. In the absence of insulator, the normalized mean length of the nanotubes remains constant (Fig. 5a(i)). In the presence of a constant amount of insulator genelet (65 nM), we varied the total tile concentration between 750 nM and 1.5 μM (Fig. 5a(ii)–(iv)). In all cases, the mean nanotube length decreases as the oscillator reaction starts and the fraction of active SW21 increases (and thus the invader transcription rate increases). The decrease in mean length is less pronounced when the total tile concentration is increased. As the fraction of active SW21 decreases, we observed that nanotubes either do not regrow (750 nM tile sample) or they regrow (1 μM and 1.5 μM tile samples). The samples with 1 μM and 1.5 μM tile concentration show that the first peak of the oscillator causes nanotubes to disassemble, and the first well enables their regrowth (see Supplementary Section 4.13 for details). We fitted the normalized nanotube mean length data and oscillator data using a sinusoidal function with exponentially damped amplitude and frequency, whose frequency and damping coefficients were constrained to be in a comparable range for both nanotube mean length and oscillator data. These phenomenological fits support our claim that one damped oscillation is observed in the nanotube mean length (Supplementary Section 5.1).

In a second series of experiments (experiment round 2), we aimed at testing the system when the oscillator exhibits two oscillations. Given a fixed total tile concentration of 1 μM, we varied the total insulator concentration. These experiments highlighted another calibration tradeoff: nanotubes weakly coupled to the oscillator do not exhibit significant mean length oscillation, but neither do nanotubes strongly coupled to the oscillator, because strong coupling perturbs the oscillator behaviour to the point where two oscillations can be barely identified (Supplementary Fig. 53). However, as shown in Fig. 5b, at intermediate coupling strength (70 nM and 100 nM insulator), the nanotubes disassemble as the oscillator reaches its first peak, and regrow as the oscillator reaches its first well. During the second peak of the oscillator, nanotube growth stalls for about 1 h before increasing again; although coupling is weaker at the second peak, the oscillator has a clear effect on nanotube mean length, which would continue to increase in the absence of insulator. In addition to the phenomenological oscillatory fit (Supplementary Figs. 63 and 64), we also fitted measured cumulative distributions with exponential and Flory–Schulz cumulative distribution functions[56] to verify whether the mean length fluctuations correspond to an overall fluctuation of the length distribution (Supplementary Section 5.3). These distributions depend on a single fitted parameter λ, which determines both mean and variance. We observe fluctuations in the values of fitted λ that are consistent with the empirical mean fluctuations.

In a third series of experiments (experiment round 3), we used a new batch of RNase H and nanotubes assembled from a tile variant (Supplementary Fig. 1) that did not exhibit excessive growth when incubated with the oscillator (Fig. 5c(i)). (We attribute this lack of overgrowth to the presence of the TAMRA fluorophore on one of the sticky ends of the tile, rather than on the central strand.) The results in Fig. 5c(ii),(iii) show that this particular nanotube variant is very sensitive to small changes in the concentration of insulator, which was varied between 34 and 40 nM. Consistently with previous experiments, in Fig. 5c(ii),(iii) we see that the mean length decreases at the first peak of the oscillator. As the oscillator trace starts decreasing towards its first well, the mean length increases. At the beginning of the second peak, the growth stalls. At 34 nM insulator, the mean length eventually increases again, while at 37 nM insulator the mean length remains low. At 40 nM insulator the nanotubes break completely during the first peak of the oscillator, and their number remains low throughout the experiment, preventing us from building mean length plots. Thus, we only show representative images of the nanotube samples at different points in time in Fig. 5d: during the oscillator peaks very few short nanotubes are visible (points ii, iii, and vi), while during the first well (point v) and at the end of the experiment several long nanotubes can be found in the imaging area. Additional images and a repeat are shown in Supplementary Figs. 57–59.

The difficulty in obtaining a marked decrease in mean nanotube length during the second peak of the oscillator in experiment rounds 2 and 3 prompted us to re-examine the behaviour of the insulator coupled to the nanotubes in the absence of oscillator. Control experiments in Supplementary Section 4.12.1 show that activation of the insulator does not result in a significant decrease of nanotube mean length after the nanotubes have been incubated in transcription mix for several hours, and that this cannot be attributed to loss of activity of RNAP, but rather to the build-up of RNA products transcribed by RNAP from the nanotubes, which may interact with and annihilate the invader or the tile toeholds[49]. In the context of oscillator experiments, over time the increase in RNA products transcribed from the nanotubes may reduce the efficiency and speed of invasion. This issue appears mitigated when the number of nanotubes is low throughout the experiment, like in experiment round 3 at 40 nM insulator (Fig. 5d).

Simultaneous modelling of coupled DNA reaction networks and nanotube self-assembly. We developed a coarse-grained model of ordinary differential equations (ODEs) that captures the evolution of nanotube length distribution, both in isolation and in the presence of molecular circuits directing assembly and disassembly[57,58]. The nanotube population is segmented into length bins, where the bin width defines the model granularity. We then approximate the number of nanotubes in the ith bin with the continuous variable L_i representing the concentration of nanotubes in the bin. Variations in L_i are caused by nanotube growth or disassembly, which can be macroscopically modelled using a series of chemical reactions. The concentration of free tiles T and of nucleated tiles L_0 are included as variables in the model.

Phenomenological reactions considered in the model are nucleation, polymerization and depolymerization, joining and fragmentation. In addition, we include reactions of invasion and anti-invasion, which affect both the concentration of free tiles and the concentration of nanotubes of any length. A thorough description of the model derivation and a discussion of its granularity are provided in Supplementary Section 5.4.

We fitted the cumulative distributions measured in experiments testing subsequent cycles of invasion and anti-invasion (Fig. 2d). The simulated result of nanotube mean length from our model is shown in Fig. 6a. The corresponding length distributions, as well as plots of free tile concentration and other relevant variables, are provided in
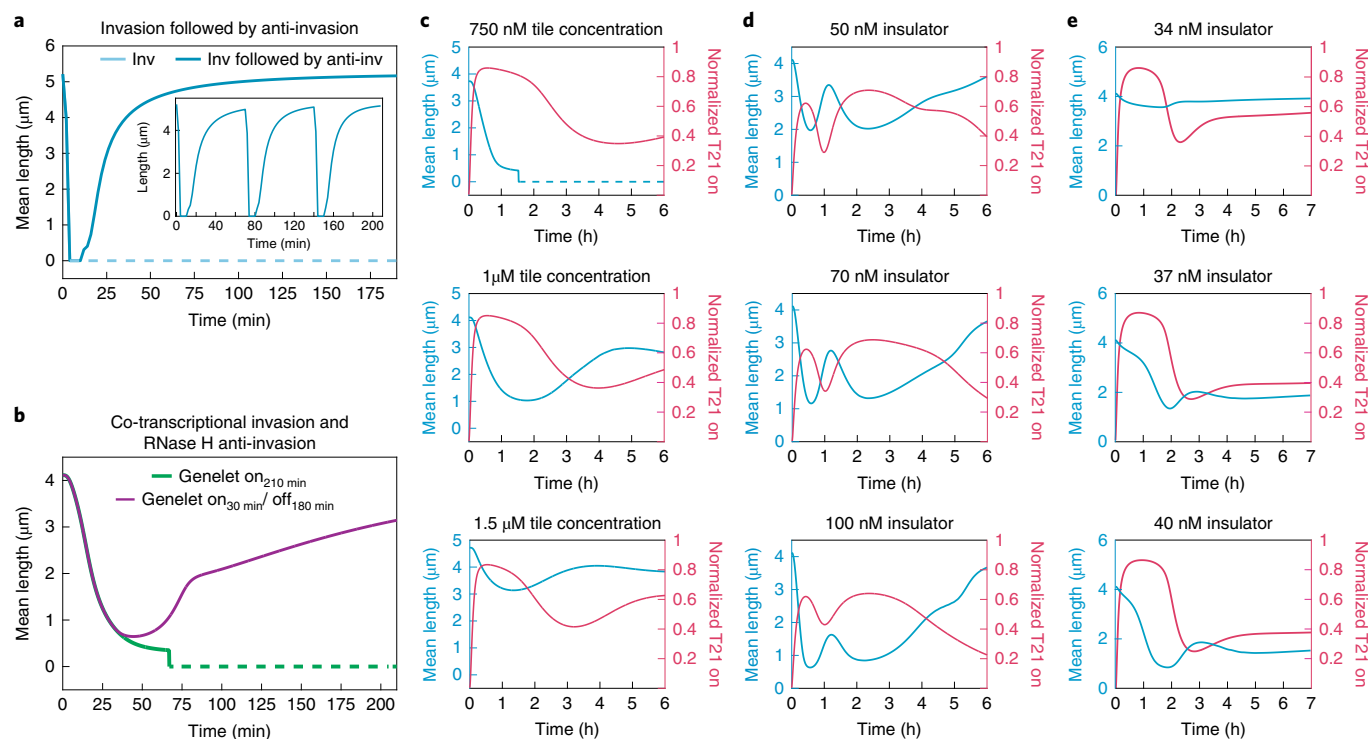
Fig. 6 | Modelling dynamic control of DNA nanotube mean length. Simulations were done using the coarse-grained model described in Supplementary Sections 5.4 and 5.5. Dashed lines indicate that no nanotubes are predicted to be present. **a**, Nanotube mean length before and after invasion and/or anti-invasion reactions, with simulation conditions reproducing the experiments in Fig. 2a(iii) where all tiles have a toehold (1 μM tiles, invader and anti-invader exceed tile concentration by 5% and 10%, respectively). Inset, cycles of invasion and anti-invasion under conditions identical to the experiments in Fig. 2d. **b**, Co-transcriptional invasion and RNase H-mediated anti-invasion, obtained by fitting the anti-invasion experiments shown in Fig. 3c,d. **c**, Simulation of experiment round 1: the total tile concentration is titrated while maintaining a constant insulator amount (experiments in Fig. 5a). The parameters used to integrate the oscillator ODEs were fitted to experimental data; in contrast, the nanotube mean length is predicted based on parameters obtained by fitting co-transcriptional experiments (Fig. 3c,d). **d**, Simulation of experiment round 2: the insulator concentration is varied, while the total tile concentration is kept constant at 1 μM. Oscillator trajectories were fitted (data in Fig. 5b), and the nanotube mean length was predicted (model parameters fitted to data in Fig. 3c,d). **e**, Simulation of experiment round 3 (Fig. 5c,d): the insulator concentration is varied in the range 34–40 nM; the sensitivity of the system to this small change in insulator concentration was captured by introducing a phenomenological sequestration rate for the invader species (Supplementary Section 5.6.2).

Supplementary Fig. 71. Fitted parameters are generally comparable to those estimated for the corresponding phenomena using different modelling techniques (cf. Supplementary Table 11 and the discussion in Supplementary Section 5.4.4)[32,44,45,59,60]. With these simulations we also computed estimates of nanotube density that are close to our observations, as shown in Supplementary Fig. 72.

This coarse-grained model can be immediately integrated with existing ODE models for DNA strand displacement systems and transcriptional networks[61–63]. To model the co-transcriptional invasion experiments shown in Fig. 3c,d we built a set of ODEs capturing activation and inhibition of a synthetic genelet, production of RNA invader, invasion reactions and RNase H-mediated anti-invasion (Supplementary Section 5.4.2). Because of the new tile architecture in these experiments, we obtained a new set of parameters for nanotube growth, as well as invasion and anti-invasion (Supplementary Table 12). The parameters for enzymes were fit, while the genelet activation and inhibition parameters were assumed to be identical to those in ref. [50] (Supplementary Table 13). Numerical simulation results (Fig. 6b) are compared to the experimental data in Supplementary Section 5.4.5 (Supplementary Fig. 73). Nanotube density estimates generally agree with measurements, although they were not taken into account in the fitting process (Supplementary Fig. 74).

To simulate the oscillator-directed nanotube assembly experiments, we revised and fitted the ODE model of our transcriptional oscillator, which was developed and refined in a series of earlier

papers[28,50,53]. The oscillator model (Supplementary Sections 5.5 and 5.6) was fitted to experimental data by assuming a simplified scenario where, rather than modelling the nanotube distribution, we included only active (free) or inactive (bound to the invader) tiles. While we did not model the production of unwanted transcripts from DNA nanotubes[49], we modelled the RNAP–tile interactions observed in control experiments (Supplementary Section 4.11.1) by assuming tiles have a weak binding affinity for free RNAP. Our fits improved after inclusion of a fitted exponential factor modelling decay of enzyme activity, suggesting that loss of enzyme activity during the reaction may be responsible for the difficulty in achieving multiple, high-amplitude oscillations[53]. The parameters obtained for each experiment round are reported in Supplementary Tables 14–16. These parameters were then used to integrate simultaneously the oscillator model and the coarse-grained nanotube distribution model developed for the co-transcriptional invasion experiments, as described in Supplementary Section 5.6.2. The simulated experimental rounds testing tile titration (keeping the insulator concentration constant) and insulator titration (keeping the tile concentration constant) are shown in Fig. 6c–e, respectively. The integrated model simulations reproduce reasonably well the trends observed in the experiments, and provide a sensible validation of our coarse-grained model. One notable discrepancy between simulations and experiments is that the model does not capture the higher growth rate of nanotubes

observed during oscillator-directed assembly experiment rounds 1 and 2 (Supplementary Sections 4.13 and 5.2.1): indeed, the coarse-grained model was trained on co-transcriptional invasion and RNase H-mediated anti-invasion, where the mean length saturates after 10 h (Supplementary Fig. 42). Simulations of experiment round 3 were able to capture the sensitivity of the system to small changes in insulator concentration only after inclusion of a phenomenological titration reaction of the invader (Supplementary Section 5.6.2). This reaction was introduced to model in a simple manner potential interactions between the invader and RNA molecules produced by transcription of the nanotubes.

Conclusions and outlook. The self-assembly of micrometre-sized DNA nanostructures was dynamically and reversibly controlled in a programmable manner using instructions encoded in other nucleic acid strands and circuits. Nanotube-forming DNA tiles include toeholds that make inter-tile bonds accessible and therefore controllable by other DNA or RNA input strands. This allowed us to control nanotube disassembly and reassembly with invader and complementary anti-invader molecules. Invader and anti-invader inputs could be released by a variety of DNA networks or molecular processes: here, we focused on transcriptional networks and we showed that an artificial transcriptional oscillator can be used to direct DNA nanotube assembly. We took advantage of enzymes fueling transcriptional networks to produce RNA invaders and to degrade tile-bound invaders to restore polymerization (alternatively, RNA anti-invaders could be used to displace invaders). We also developed a mathematical model that captures variations in nanotube length distribution caused by the presence of invader and anti-invader molecules; this model can be integrated with mathematical models of any DNA chemical reaction network, including our transcriptional oscillator.

Earlier demonstrations of DNA nanostructure control using strand displacement include the contraction and relaxation of lattices[64,65] and control of the relative position of connected DNA origami components[66]. Zhang and colleagues were able to trigger DNA nanotube assembly using an enzyme-free catalytic circuit[32] via an irreversible mechanism that achieves a fixed steady state. The transcriptional oscillator used in our experiments was used to direct motion of DNA tweezers, one of the simplest molecular nanomachines[50]. This study capitalizes on earlier work to achieve coupling of a complex, autonomous circuit with a self-assembly process yielding micrometre-sized structures.

Coupling a nonlinear dynamical system with downstream pathways presents many challenges. First, it is essential to calibrate carefully the concentration of signalling components that are depleted by downstream processes simultaneously present in solution[50,55] (in our case, the DNA or RNA components of the oscillator that are expected to direct nanotube assembly). Buffering devices, such as the insulator genelet we employed, can mitigate this problem in cases where it is possible to sense and amplify the concentration of a critical component[50,67]. Phosphorylation mechanisms and catalytic cycles may help biological cells to mitigate this issue[55]. Another challenge is posed by resource limitation: for instance, enzymes may become overloaded in the presence of too many substrates, resulting in performance degradation[68]. Competition for resources may be caused also by non-specific binding, such as non-specific transcription of RNA from the nanotubes.

Correct operation of interconnected systems is also challenged by the sensitivity of each system to perturbations. The oscillator used here is known for its sensitivity to variations in enzyme concentration and activity[53], yet alternative oscillators present challenges for coupling with DNA nanostructures. For instance, the PEN (polymerase–exonuclease–nickase) oscillators utilize DNA modifying enzymes and typically operate at high-temperature conditions that could interfere with the current DNA nanotube designs[29]. The existing demonstration of a DNA-only damped oscillator presents small amplitude and low frequency[69]. Finally, a closed system may suffer from accumulation of incorrect products, deactivated components or waste complexes, which can perturb the desired circuit kinetics[28,50,53]. Cells obtain energy from the environment and eliminate waste, and we foresee that any active biomaterial should include similar in-flux and out-flux mechanisms to sustain dynamic behaviours.

We hope that this study will find use in the design and synthesis of reconfigurable DNA biomaterials, because the invasion and anti-invasion architecture is compatible with most DNA tiling approaches[70,71] and may be extended to DNA origami tiles[72,73]. These assemblies could be engineered to respond directly or indirectly to many biochemical signals, by triggering the release of invader or anti-invader molecules via aptamers[74]. Dynamic DNA structures may be functionalized with desirable components to obtain responsive heterogeneous scaffolds[75,76]. The architecture we proposed could be adapted to obtain active behaviours in more complex materials organized by DNA such as nanoparticles[77] and droplets[78]. Ultimately, artificial dynamic nucleic acid scaffolds could be embedded and produced inside cells: cellular sensors and signal processing modules could be transduced into RNA signals and direct artificial RNA or DNA assemblies inside cells to build artificial organelles or scaffolds that could modulate metabolic pathways and potentially direct transport of components[79,80].

Methods

DNA oligonucleotides and enzymes. Oligonucleotides were purchased from IDT DNA. T7 RNAP was purchased from Cellscript, and RNase H was purchased from Thermofisher. Transcription reagents were purchased from Epicentre Biotechnologies and New England Biolabs. Oligonucleotide sequences and modifications, as well as further details on the preparation of DNA nanotubes and transcription reactions, are available in the Supplementary Information.

Fluorescence imaging. Cy3 (or Alexa 488)-labelled DNA nanotubes were imaged using an inverted epifluorescence microscope (Nikon Eclipse TI-E) with 60X/1.40 NA oil-immersion objectives. Samples containing nanotubes were imaged at 50 nM tile concentration in corresponding experimental buffer conditions. Samples were placed on a Fisherbrand microscope coverglass and covered with microslides (VWR). Nanotube length distributions were quantified using ImageJ and the plugin Skeletonize. Branching or looping nanotubes were excluded from the length data set using an in-house MATLAB script. Nanotube length distributions were monitored for 3–30 h; the results of each triplicate experiment are reported in the Supplementary Information as violin plots reporting the nanotube density.

AFM. AFM images were obtained in tapping mode with a Digital Instruments Multimode AFM equipped with a Nanoscope III controller. Sharp nitride lever tips from Bruker with a nominal spring constant of 0.24 N m^{-1} were used for imaging, with a drive frequency of 9–10 kHz. Samples were imaged using 1X TAE and 12.5 mM MgCl$_2$ buffer.

Fluorescence spectroscopy. Bulk fluorescence experiments were performed using a Horiba Fluorlog 3. Samples were placed in 60 μl quartz cuvettes (Starna Cells) and incubated in the sample chamber at 37 °C. To avoid evaporation, the sample was covered with 50 μl hexadecane (MP Biomedical). Fluorescence emission of reporters was measured over three separate experiments and averaged accordingly. Excitation/emission settings were chosen according to the recommendation of the supplier IDT DNA. Oscillator fluorescence measurements were normalized using maximal on–off fluorescence ratios as described in the Supplementary Information.

Data availability

All the data sets generated and/or analysed during this study and supporting the findings described are available within the Article and its Supplementary Information and/or from the corresponding author upon reasonable request.

References

1. Mann, S. Life as a nanoscale phenomenon. *Angew. Chem. Int. Ed.* **47**, 5306–5320 (2008).
2. Li, R. & Gundersen, G. G. Beyond polymer polarity: how the cytoskeleton builds a polarized cell. *Nat. Rev. Mol. Cell Biol.* **9**, 860–873 (2008).

3. Desai, A. & Mitchison, T. J. Microtubule polymerization dynamics. *Annu. Rev. Cell Dev. Biol.* **13**, 83–117 (1997).

4. Conde, C. & Cáceres, A. Microtubule assembly, organization and dynamics in axons and dendrites. *Nat. Rev. Neurosci.* **10**, 319–332 (2009).

5. Mattila, P. K. & Lappalainen, P. Filopodia: molecular architecture and cellular functions. *Nat. Rev. Mol. Cell Biol.* **9**, 446–454 (2008).

6. Carlson, E. D., Gan, R., Hodgman, C. E. & Jewett, M. C. Cell-free protein synthesis: applications come of age. *Biotechnol. Adv.* **30**, 1185–1194 (2012).

7. Zhang, F., Nangreave, J., Liu, Y. & Yan, H. Structural DNA nanotechnology: state of the art and future perspective. *J. Am. Chem. Soc.* **136**, 11198–11211 (2014).

8. Blind, M. & Blank, M. Aptamer selection technology and recent advances. *Mol. Ther. Nucleic Acids* **4**, e223 (2015).

9. Zhang, D. Y. & Seelig, G. Dynamic DNA nanotechnology using strand-displacement reactions. *Nat. Chem.* **3**, 103–113 (2011).

10. Douglas, S. M. et al. Rapid prototyping of 3D DNA-origami shapes with caDNAno. *Nucleic Acids Res.* **37**, 5001–5006 (2009).

11. Zadeh, J. N. et al. Nupack: analysis and design of nucleic acid systems. *J. Comput. Chem.* **32**, 170–173 (2011).

12. Fu, T. & Seeman, N. DNA double-crossover molecules. *Biochemistry* **32**, 3211–3220 (1993).

13. Winfree, E., Liu, F., Wenzler, L. A. & Seeman, N. C. Design and self-assembly of two-dimensional DNA crystals. *Nature* **394**, 539–544 (1998).

14. Rothemund, P. W. K. et al. Design and characterization of programmable DNA nanotubes. *J. Am. Chem. Soc.* **126**, 16344–16352 (2004).

15. Rothemund, P. W. Folding DNA to create nanoscale shapes and patterns. *Nature* **440**, 297–302 (2006).

16. Douglas, S. M. et al. Self-assembly of DNA into nanoscale three-dimensional shapes. *Nature* **459**, 414–418 (2009).

17. Ke, Y., Ong, L. L., Shih, W. M. & Yin, P. Three-dimensional structures self-assembled from DNA bricks. *Science* **338**, 1177–1183 (2012).

18. Zhang, F. et al. Complex wireframe DNA origami nanostructures with multi-arm junction vertices. *Nat. Nanotechnol.* **10**, 779–784 (2015).

19. Benson, E. et al. DNA rendering of polyhedral meshes at the nanoscale. *Nature* **523**, 441–444 (2015).

20. Zheng, J. et al. From molecular to macroscopic via the rational design of a self-assembled 3D DNA crystal. *Nature* **461**, 74–77 (2009).

21. Jones, M. R., Seeman, N. C. & Mirkin, C. A. Programmable materials and the nature of the DNA bond. *Science* **347**, 1260901 (2015).

22. Yurke, B. & Mills, A. P. Using DNA to power nanostructures. *Genet. Program. Evol. M.* **4**, 111–122 (2003).

23. Seelig, G., Soloveichik, D., Zhang, D. Y. & Winfree, E. Enzyme-free nucleic acid logic circuits. *Science* **314**, 1585–1588 (2006).

24. Qian, L. & Winfree, E. Scaling up digital circuit computation with DNA strand displacement cascades. *Science* **3**, 1196–1201 (2011).

25. Chen, Y.-J. et al. Programmable chemical controllers made from DNA. *Nat. Nanotechnol.* **8**, 755–762 (2013).

26. Li, B., Ellington, A. D. & Chen, X. Rational, modular adaptation of enzyme-free DNA circuits to multiple detection methods. *Nucleic Acids Res.* **39**, e110 (2011).

27. Kim, J., White, K. S. & Winfree, E. Construction of an in vitro bistable circuit from synthetic transcriptional switches. *Mol. Syst. Biol.* **2**, 68 (2006).

28. Kim, J. & Winfree, E. Synthetic in vitro transcriptional oscillators. *Mol. Syst. Biol.* **7**, 465 (2011).

29. Montagne, K., Plasson, R., Sakai, Y., Fujii, T. & Rondelez, Y. Programming an in vitro DNA oscillator using a molecular networking strategy. *Mol. Syst. Biol.* **7**, 466 (2011).

30. Padirac, A., Fujii, T. & Rondelez, Y. Bottom-up construction of in vitro switchable memories. *Proc. Natl Acad. Sci. USA* **109**, E3212–E3220 (2012).

31. Ekani-Nkodo, A., Kumar, A. & Fygenson, D. K. Joining and scission in the self-assembly of nanotubes from DNA tiles. *Phys. Rev. Lett.* **93**, 268301 (2004).

32. Zhang, D. Y., Hariadi, R. F., Choi, H. M. T. & Winfree, E. Integrating DNA strand-displacement circuitry with DNA tile self-assembly. *Nat. Commun.* **4**, 1965 (2013).

33. Amodio, A., Adedeji, A. F., Castronovo, M., Franco, E. & Ricci, F. pH-controlled assembly of DNA tiles. *J. Am. Chem. Soc.* **138**, 12735–12738 (2016).

34. Green, L. N., Amodio, A., Subramanian, H. K. K. S., Ricci, F. & Franco, E. pH-driven reversible self-assembly of micron-scale DNA scaffolds. *Nano Lett.* **17**, 7283–7288 (2017).

35. Jeong, B. & Gutowska, A. Lessons from nature: stimuli-responsive polymers and their biomedical applications. *Trends Biotechnol.* **20**, 305–311 (2002).

36. Szostak, J. W., Bartel, D. P. & Luisi, P. L. Synthesizing life. *Nature* **409**, 387–390 (2001).

37. Phillips, J. A. et al. Using azobenzene incorporated DNA aptamers to probe molecular binding interactions. *Bioconjug. Chem.* **22**, 282–288 (2011).

38. He, X. et al. Synthetic homeostatic materials with chemo-mechano-chemical self-regulation. *Nature* **487**, 214–218 (2012).

39. Chr'etien, D. & Wade, R. H. New data on the microtubule surface lattice. *Biol. Cell* **71**, 161–174 (1991).

40. Wade, R. H., Chr´etien, D. & Job, D. Characterization of microtubule protofilament numbers: how does the surface lattice accommodate? *J. Mol. Biol.* **212**, 775–786 (1990).

41. Gittes, F., Mickey, B., Nettleton, J. & Howard, J. Flexural rigidity of microtubules and actin filaments measured from thermal fluctuations in shape. *J. Cell Biol.* **120**, 923–934 (1993).

42. Mohammed, A. M. & Schulman, R. Directing self-assembly of DNA nanotubes using programmable seeds. *Nano Lett.* **13**, 4006–4013 (2013).

43. Oosawa, F. et al. *Thermodynamics of the Polymerization of Protein* (Academic Press, Cambridge, 1975).

44. Hariadi, R. F., Yurke, B. & Winfree, E. Thermodynamics and kinetics of DNA nanotube polymerization from single-filament measurements. *Chem. Sci.* **6**, 2252–2267 (2015).

45. Evans, C. G., Hariadi, R. F. & Winfree, E. Direct atomic force microscopy observation of DNA tile crystal growth at the single-molecule level. *J. Am. Chem. Soc.* **134**, 10485–10492 (2012).

46. Zhang, D. Y. & Winfree, E. Robustness and modularity properties of a non-covalent DNA catalytic reaction. *Nucleic Acids Res.* **38**, 4182–4197 (2010).

47. Evangelista, M., Zigmond, S. & Boone, C. Formins: signaling effectors for assembly and polarization of actin filaments. *J. Cell Sci.* **116**, 2603–2611 (2003).

48. Kim, J. *In Vitro Synthetic Transcriptional Networks.* PhD thesis, California Institute of Technology (2007).

49. Schaffter, S. et al. T7 RNA polymerase non-specifically transcribes and induces disassembly of DNA nanostructures. *Nucleic Acids Res.* **46**, 5332–5343 (2018).

50. Franco, E. et al. Timing molecular motion and production with a synthetic transcriptional clock. *Proc. Natl Acad. Sci. USA* **108**, E784–E793 (2011).

51. Rahi, S. J., Pecani, K., Ondracka, A., Oikonomou, C. & Cross, F. R. The CFK-APC/C oscillator predominantly entrains periodic cell-cycle transcription. *Cell* **165**, 475–487 (2016).

52. Huang, C.-H., Tang, M., Shi, C., Iglesias, P. A. & Devreotes, P. N. An excitable signal integrator couples to an idling cytoskeletal oscillator to drive cell migration. *Nat. Cell Biol.* **15**, 1307–1316 (2013).

53. Weitz, M. et al. Diversity in the dynamical behaviour of a compartmentalized programmable biochemical oscillator. *Nat. Chem.* **6**, 295–302 (2014).

54. Cuba Samaniego, C., Giordano, G., Kim, J., Blanchini, F. & Franco, E. Molecular titration promotes oscillations and bistability in minimal network models with monomeric regulators. *ACS Synth. Biol* **5**, 321–333 (2016).

55. Del Vecchio, D., Ninfa, A. J. & Sontag, E. D. Modular cell biology: retroactivity and insulation. *Mol. Syst. Biol.* **4**, 161 (2008).

56. Israelachvili, J. N. *Intermolecular and Surface Forces* revised 3rd edn (Academic Press, Cambridge, 2011).

57. Mardanlou, V. et al. A coarse-grained model of DNA nanotube population growth in *International Conference on DNA-Based Computers*, 135–147 (Springer, 2016).

58. Mardanlou, V. et al. A coarse-grained model captures the temporal evolution of DNA nanotube length distributions. *Nat. Comput.* **17**, 183–199 (2018).

59. Hariadi, R. F., Winfree, E. & Yurke, B. Determining hydrodynamic forces in bursting bubbles using DNA nanotube mechanics. *Proc. Natl Acad. Sci. USA* **112**, E6086–E6095 (2015).

60. Schulman, R. & Winfree, E. Synthesis of crystals with a programmable kinetic barrier to nucleation. *Proc. Natl Acad. Sci. USA* **104**, 15236–15241 (2007).

61. Qian, L. & Winfree, E. A simple DNA gate motif for synthesizing large-scale circuits. *J. R. Soc. Interface* **8**, 1281–1297 (2011).

62. Soloveichik, D., Seelig, G. & Winfree, E. DNA as a universal substrate for chemical kinetics. *Proc. Natl Acad. Sci. USA* **107**, 5393–5398 (2010).

63. Kim, J., Hopfield, J. & Winfree, E. Neural network computation by in vitro transcriptional circuits in *Advances in Neural Information Processing Systems* 681–688 (NIPS Foundation, 2004).

64. Feng, L., Park, S. H., Reif, J. H. & Yan, H. A two-state DNA lattice switched by DNA nanoactuator. *Angew. Chem. Int. Ed.* **115**, 4342–4346 (2003).

65. Aldaye, F. A. & Sleiman, H. F. Dynamic DNA templates for discrete gold nanoparticle assemblies: control of geometry, modularity, write/erase and structural switching. *J. Am. Chem. Soc.* **129**, 4130–4131 (2007).

66. Gerling, T., Wagenbauer, K. F., Neuner, A. M. & Dietz, H. Dynamic DNA devices and assemblies formed by shape-complementary, non–base pairing 3D components. *Science* **347**, 1446–1452 (2015).

67. Mishra, D., Rivera, P. M., Lin, A., Del Vecchio, D. & Weiss, R. A load driver device for engineering modularity in biological networks. *Nat. Biotechnol.* **32**, 1268–1275 (2014).

68. Rondelez, Y. Competition for catalytic resources alters biological network dynamics. *Phys. Rev. Lett.* **108**, 018102 (2012).

69. Srinivas, N., Parkin, J., Seelig, G., Winfree, E. & Soloveichik, D. Enzyme-free nucleic acid dynamical systems. *Science* **358**, eaal2052 (2017).

70. Yan, H., Park, S. H., Finkelstein, G., Reif, J. H. & LaBean, T. H. DNA-templated self-assembly of protein arrays and highly conductive nanowires. *Science* **301**, 1882–1884 (2003).

71. LaBean, T. H. et al. Construction, analysis, ligation, and self-assembly of DNA triple crossover complexes. *J. Am. Chem. Soc.* **122**, 1848–1860 (2000).

72. Zhao, Z., Liu, Y. & Yan, H. Organizing DNA origami tiles into larger structures using preformed scaffold frames. *Nano Lett.* **11**, 2997–3002 (2011).

73. Woo, S. & Rothemund, P. W. K. Programmable molecular recognition based on the geometry of DNA nanostructures. *Nat. Chem* **3**, 620–627 (2011).

74. Cho, E. J., Lee, J.-W. & Ellington, A. D. Applications of aptamers as sensors. *Annu. Rev. Anal. Chem.* **2**, 241–264 (2009).

75. Sharma, J. et al. Control of self-assembly of DNA tubules through integration of gold nanoparticles. *Science* **323**, 112–116 (2009).

76. Liu, D., Park, S. H., Reif, J. H. & LaBean, T. H. DNA nanotubes self-assembled from triple-crossover tiles as templates for conductive nanowires. *Proc. Natl Acad. Sci. USA* **101**, 717–722 (2004).

77. O' Brien, M. N., Jones, M. R., Lee, B. & Mirkin, C. A. Anisotropic nanoparticle complementarity in DNA-mediated co-crystallization. *Nat. Mater.* **14**, 833–839 (2015).

78. Hadorn, M. et al. Specific and reversible DNA-directed self-assembly of oil-in-water emulsion droplets. *Proc. Natl Acad. Sci. USA* **109**, 20320–20325 (2012).

79. Hariadi, R. F., Appukutty, A. J. & Sivaramakrishnan, S. Engineering circular gliding of actin filaments along myosin-patterned DNA nanotube rings to study long-term actin–myosin behaviors. *ACS Nano* **10**, 8281–8288 (2016).

80. Delebecque, C. J., Lindner, A. B., Silver, P. A. & Aldaye, F. A. Organization of intracellular reactions with rationally designed RNA assemblies. *Science* **333**, 470–474 (2011).

Acknowledgements

Author contributions
E.F., J.K. and R.F.H. conceived and designed research and analysed the data. L.N.G. and H.K.K.S. designed and performed the experiments and analysed the data. V.M. and J.K. performed numerical simulations. E.F., L.N.G. and H.K.K.S. co-wrote the paper.

Competing interests
The authors declare no competing interests.

Additional information
Supplementary information is available for this paper at https://doi.org/10.1038/s41557-019-0251-8.

Reprints and permissions information is available at www.nature.com/reprints.

Correspondence and requests for materials should be addressed to E.F.

Publisher's note: Springer Nature remains neutral with regard to jurisdictional claims in published maps and institutional affiliations.